

HandCept: A Visual-Inertial Fusion Framework for Accurate Proprioception in Dexterous Hands

Junda Huang¹, Jianshu Zhou², *Member, IEEE*, Honghao Guo¹, and Yunhui Liu¹, *Fellow, IEEE*

Abstract—As robotics progresses toward general manipulation, dexterous hands are becoming increasingly critical. However, proprioception in dexterous hands remains a bottleneck due to limitations in volume and generality. In this work, we present HandCept, a novel visual-inertial proprioception framework designed to overcome the challenges of traditional joint angle estimation methods. HandCept addresses the difficulty of achieving accurate and robust joint angle estimation in dynamic environments where both visual and inertial measurements are prone to noise and drift. It leverages a zero-shot learning approach using a wrist-mounted RGB-D camera and 9-axis IMUs, fused in real time via a latency-free Extended Kalman Filter (EKF). Our results show that HandCept achieves joint angle estimation errors between 2° and 4° without observable drift, outperforming visual-only and inertial-only methods. Furthermore, we validate the stability and uniformity of the IMU system, demonstrating that a common base frame across IMUs simplifies system calibration. To support sim-to-real transfer, we also open-sourced our high-fidelity rendering pipeline, which is essential for training without real-world ground truth. This work offers a robust, generalizable solution for proprioception in dexterous hands, with significant implications for robotic manipulation and human-robot interaction.

Index Terms—Proprioception, Dexterous Hand, Visual-Inertial Fusion.

I. INTRODUCTION

Robots are increasingly being deployed in a wide range of diverse tasks and are expected to operate in unstructured environments such as homes, shopping malls, and hospitals [1], [2]. Performing these tasks often involves manipulation—either bimanual or in-hand dexterous manipulation—to interact with the environment. The end-effector plays a fundamental role in enabling such robotic manipulation [3]–[5]. Recent advances in dexterous hands [6] and two-finger grippers [7] across various applications have demonstrated the potential and importance of further developing dexterous hands. However, due to limitations in proprioceptive frameworks, many innovative dexterous hand designs remain confined to demonstrations of structural dexterity or teleoperated in open-loop [8]–[11].

To address the challenges of proprioception in dexterous hands, we propose HandCept, a proprioceptive framework for

This work is supported by the CUHK T Stone Robotics Institute, in part by the InnoHK initiative of the Innovation and Technology Commission of the Hong Kong Special Administrative Region Government via the Hong Kong Centre for Logistics Robotics, and in part by the HK RGC under GRF-14207423.

¹Authors with the Department of Mechanical and Automation Engineering, The Chinese University of Hong Kong.

²Authors with the Department of Mechanical Engineering, University of California, Berkeley.

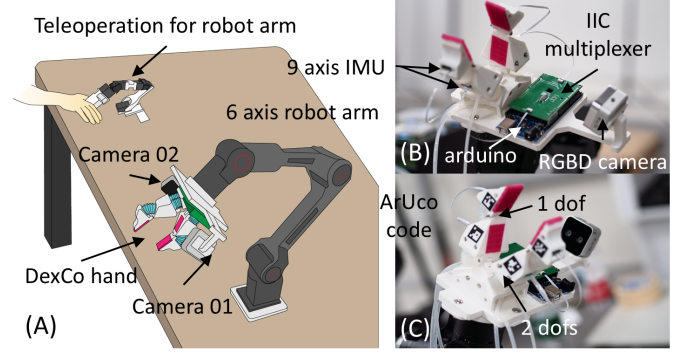


Fig. 1. (A) Overview of the HandCept implementation on the DexCo hand [8]. (B) and (C) show the physical DexCo hand; ArUco markers in (C) are used in experiment to obtain ground truth poses for each link.

estimating joint angles in dexterous hands with rigid links. HandCept combines visual and inertial pose estimation to infer joint angles and consists of both hardware and algorithmic components. On the hardware side, we design a compact 9-axis IMU system suitable for integration into the confined spaces of dexterous hands. By optimizing circuitry, communication, and control, the resulting IMU module achieves the smallest known form factor (12 mm \times 15 mm). Unlike conventional IMU applications, dexterous hands often consist of multiple serial and parallel link structures. Accordingly, our IMU system supports scalable integration via both serial and parallel configurations, making it adaptable to various dexterous hand designs or even robotic arms with differing numbers of fingers and links.

On the algorithmic side, we introduce a kinematics-constrained estimation algorithm to eliminate spatial redundancy between inertial and visual pose predictions. In contrast to typical visual estimation algorithms that rely on mixed real and synthetic datasets, our pose estimation network is trained entirely on high-fidelity synthetic data generated via Blender with zero-shot sim2real. We open-source this rendering pipeline to provide the community with a reproducible, high-fidelity simulation method. Finally, we propose a fusion method based on an Extended Kalman Filter (EKF) to address the latency between the two sensing modalities.

Experimental results validate the feasibility, reliability, and advantages of both the hardware and software components of HandCept. Comparative studies demonstrate a state of the art result that HandCept provides long-term, robust proprioception, maintaining joint angle estimation errors up to 2° .

The remainder of this paper is organized as follows: Section

II reviews related work. Section III provides an overview of the HandCept framework and its core principles. Section IV details the link pose estimation methods. Section V presents the EKF-based sensor fusion algorithm. Section VI reports the experimental validation of HandCept’s performance and key assumptions. Finally, Section VII discusses and summarizes the findings and outlines future research directions.

II. RELATED WORKS

A. Joint Perception for Dexterous Hand

Recent advances in the design of dexterous hands have made traditional joint perception methods increasingly inadequate for supporting more diverse and flexible hand architectures[8], [12]. Generally, joint position sensing in dexterous hands falls into two main categories: encoder-based and tendon-driven approaches. Encoder-based solutions [11], [13], [14] provide direct and highly accurate feedback; however, the physical size of the encoders imposes constraints on miniaturization and prevents the integration of multiple degrees of freedom within a single joint. On the other hand, tendon-driven dexterous hands [6], [12], [15], [16] estimate joint positions indirectly, but suffer from disadvantages in terms of stability, precision, and ease of maintenance.

Several novel approaches have also been proposed for joint or bending sensing, including the use of optical fibers [17], [18], inductive sensors [19], capacitive sensors [20], magnetic field measurements [21], vision-based systems [22], and fluidic sensors [23], [24]. However, these methods are not yet suitable for practical deployment in manipulation tasks due to limitations in robustness, accuracy, or integration complexity.

B. Visual-Inertial Perception

Visual-inertial perception has been extensively applied in the field of locomotion, where the primary objective is the localization of a single mobile system [25], [26]. More complex applications can be found in VR-based hand tracking systems [27], [28], which emphasize generalizability and visual interactive properties. However, such general-purpose designs often fall short in meeting the demands of robotic manipulation tasks, which require high precision, robustness, long-term reliability, and maintainability. Consequently, these systems cannot be directly transferred to robotic settings that demand task-level accuracy and consistent performance.

III. HANDCEPT FRAMEWORK OVERVIEW

HandCept is a proprioception framework designed to estimate joint angles—that is, the configuration space—of dexterous robotic hands. In recent years, a wide variety of dexterous hand designs have emerged, incorporating diverse actuation topologies such as roller joints, prismatic joints, compliant joints, soft joints, functional joints, and transformable joints. Despite this diversity, HandCept is primarily tailored for dexterous hands with revolute joint chain topologies, which are not only the most prevalent in modern robotic designs but also closely resemble the actuation structures observed in biological systems. Notably, revolute joint chains can integrate

compliant, universal, or transformable joints, as their joint angles can still be inferred from the 3D poses of associated rigid links.

HandCept adopts a model-based approach to proprioception, as illustrated in Fig. 2. The system leverages two sensory modalities—inertial and visual—that together contribute to estimating the pose of each rigid link within the dexterous hand. The inertial component, derived from multiple 9-axis IMUs, captures the 3D orientation (rotation) of each link. The visual component, provided by a wrist-mounted RGB-D camera, estimates the full 6D pose (rotation and translation) of the links. The design and implementation details of the 9-axis IMUs are elaborated in a subsequent section.

The visual estimation component is based on FFB6D, an instance-level object pose estimation algorithm that produces segmentation masks, keypoints, and 6D poses for all objects within an input image. Given the lack of accessible ground-truth data for many dexterous hands, we developed a dedicated Blender-based simulation pipeline to generate high-quality synthetic training data, enabling zero-shot sim-to-real transfer for the FFB6D model. The initial 6D pose estimates from FFB6D are further refined using kinematic constraints derived from the known topology of the hand, thereby improving the accuracy of the visual estimates. These refined visual estimates are then used to calibrate the inertial measurements, aligning both modalities to a unified reference frame. Finally, the visual and inertial data are fused using an Extended Kalman Filter (EKF), resulting in robust, drift-free, and accurate 3D pose estimates for each link. These fused 3D poses are used to compute the joint angles of the dexterous hand, thus enabling accurate proprioception.

IV. RIGID BODY POSE ESTIMATION

In this section, we outline the methods employed to estimate the poses from both inertial and visual systems. Unlike general-purpose algorithms designed to estimate the 6D pose of arbitrary objects, robotic systems typically consist of tree-like structures, where kinematic constraints among connected rigid bodies play a critical role. Consequently, incorporating these kinematic constraints into the pose estimation process is essential. It is important to note that this work focuses exclusively on systems with revolute joint chains; other joint types (e.g., prismatic or soft joints) are not considered.

A. Inertial-based SO3 Estimation

The IMU system is designed to support both serial and parallel extensibility. Using the I²C protocol, IMU PCBs can be serially connected to extend the system, while a custom-designed I²C multiplexer enables parallel connections to accommodate different numbers of dexterous fingers or limbs (Fig. 3A). This IMU system is also the smallest known design, facilitating easy integration into dexterous hands while maintaining a real-time update frequency of $\geq 200\text{Hz}$ (Fig. 3B). Utilizing 9-axis IMUs is essential for pose estimation, as it reduces the calibration burden. Given the compactness of dexterous hands, the magnetic field can be assumed uniform across all IMUs, allowing the use of a common base frame

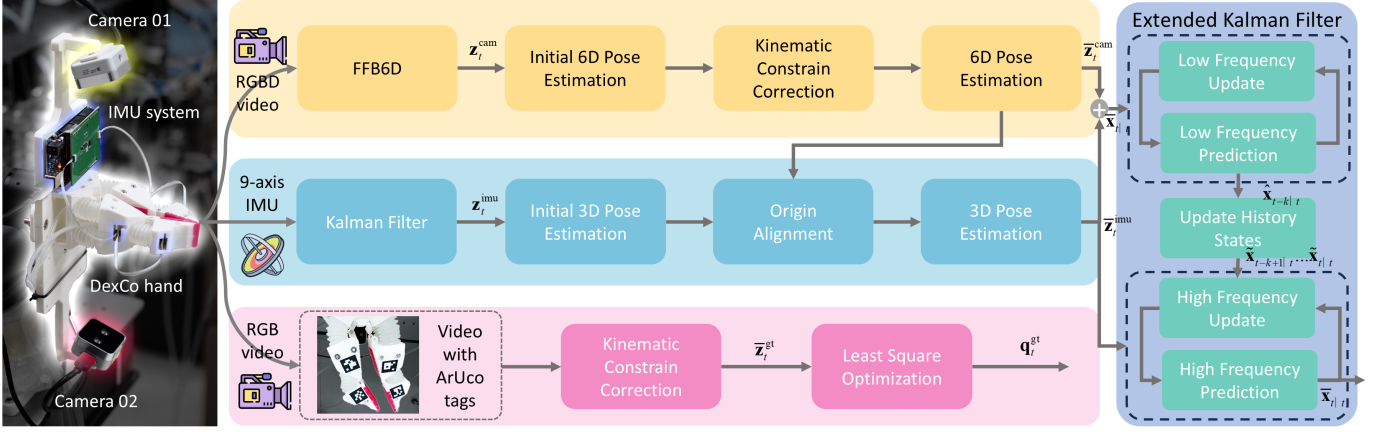


Fig. 2. Algorithmic pipeline of HandCept. The ArUco code-based ground truth system is used solely for experimental validation. HandCept estimates the joint angles of the DexCo hand by fusing visual and inertial data streams. The pose estimates are refined with kinematic constraints before being fused using an Extended Kalman Filter (EKF). Due to the latency in visual processing, each visual-inertial update is used to correct the estimate at time $t + 1$, starting from k previous steps (i.e., at $t - k$). Meanwhile, IMU data provides real-time updates via the EKF.

across different modules—a condition verified in our experiments.

For the pose estimation algorithm, we leverage the inherent stability of the kalman filter, which are widely adopted for 9-axis IMU-based orientation estimation. As a result, the direct use of raw IMU data (acceleration, magnet, and angular velocity) is typically unnecessary for most orientation applications. In our framework, a kalman filter is employed to estimate the 3D orientation ($SO(3)$) of each link reliably, thereby providing robust inertial-based pose measurements, denoted as $\mathbf{z}_t^{\text{imu}}$.

Let $\{IMU_i\}$, $\{IMU_b\}$, $\{b\}$, $\{ee\}$, and $\{L_i\}$ denote the i -th IMU frame, the common IMU base frame, the robot arm’s base frame, the end-effector frame, and the i -th finger link’s frame, respectively. Let aT_b represent the homogeneous transformation matrix from frame a to frame b . The estimated transformation from the i -th IMU frame to the end-effector frame is expressed as:

$${}^{IMU_i}\hat{T}_{ee} = {}^{IMU_i}\hat{T}_{IMU_b}(\mathbf{z}_t^{\text{imu}}) {}^{IMU_b}T_b {}^bT_{ee}(\boldsymbol{\theta}) \quad (1)$$

where $\hat{(\cdot)}$ means the measured value, $\boldsymbol{\theta}$ is the joint angles of the robot arm.

B. Visual-based SE3 Estimation

The visual system leverages a wrist-mounted RGB-D camera to provide full 6D pose ($SE(3)$) estimation for each finger link. Considering it is hard for the HandCept-targeted dexterous hand to get the ground truth SE3 of each link in real scenario, we decided to purely use synthetic data for zero-shot training. The rendering algorithm based on blender performs high fidelity rendering by using both the UV wrapper and real pano background (Fig. 4A), which is also inspired by the fast growing real2sim tech. However, it’s obvious that the real-world images are clutter and noisy, while we didn’t add noise for sim2real transfer in this study.

The FFB6D [29] is used as the segmentation and 6D pose estimation algorithm, which provides instance-level prediction. A sum loss, including the segmentation loss (Focal Loss), center point loss (L1 Loss), and keypoints loss (L1 Loss),

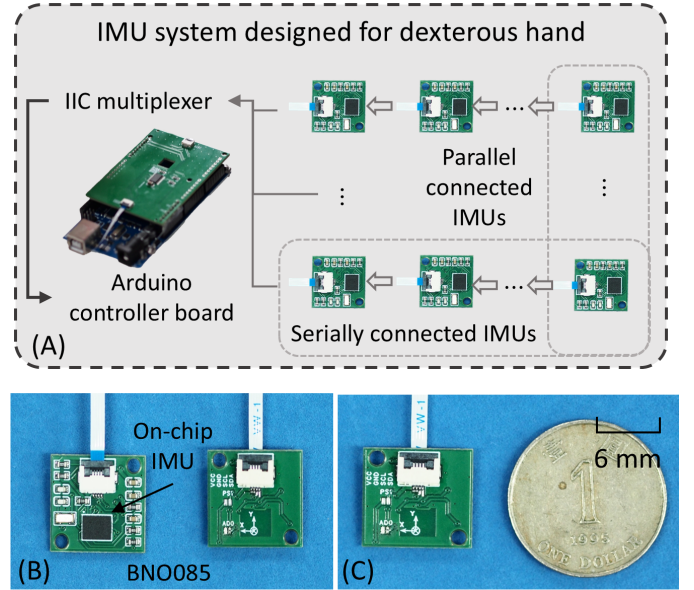


Fig. 3. (A) Architecture of the modular IMU system. Using the I²C protocol, multiple 9-axis IMUs can be connected in series to expand the system. The I²C multiplexer supports parallel connections, enabling applications such as five-fingered hands. An Arduino collects and transmits the data to a computer via a serial interface. (B) Front and back views of the designed IMU module—one of the smallest known IMU boards, offering low cost and high accuracy for general-purpose use.

are shown in the Fig. 4C in the training process. As shown in the Fig. 4B, the quantified results of visual estimations on the rendered images are highly accurate under different backgrounds, while the real images have some error.

C. Kinematics Constrains

In robotic systems, the interdependencies among the rigid bodies are governed by specific kinematic constraints determined by the revolute joint chain topology. Suppose ${}^aR_b \in SO(3)$ is the rotation matrix from frame a to frame b .

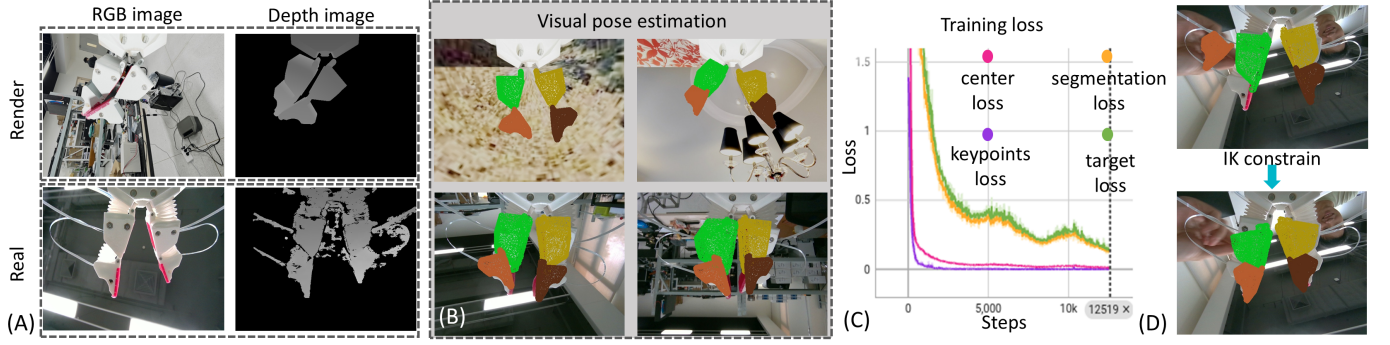


Fig. 4. (A) Comparison between high-fidelity rendered RGB-D images and real-world images. (B) Zero-shot 6D pose estimation results: the first row shows predictions on rendered images, and the second row shows predictions on real images across varying end-effector poses and hand configurations. (C) Training loss progression across four loss components. (D) Improved 6D pose estimation by enforcing kinematic constraints. Human-hand interference introduces inaccurate pose estimates, which are corrected by removing undesired rotations and translations through kinematic constraints.

Applying least square method

$$\min_{R_i} \frac{1}{2} \left\| \tilde{R} - \bar{R} \cdot R_i \right\|_F^2, \quad (2)$$

where $i \in \{x, y, z\}$ and R_i represents the rotation matrix around axis i , \tilde{R} is the observed rotation, \bar{R} is the rotation matrix considering kinematics constrain, $\|\cdot\|_F$ denotes the Frobenius norm. The extra rotation R_i can be therefore removed from the measured $\mathbf{z}_t^{\text{imu}}$.

These constraints are incorporated into the pose estimation process to enforce consistency across the chain, thereby improving the overall accuracy and stability of the estimated 6D poses (Fig. 4D).

V. FUSION USING LATENCY-FREE EKF

The Extended Kalman Filter is a powerful tool for state estimation in non-linear systems. It operates through a two-step process: prediction and update. In the prediction step, the EKF uses a system model to project the current state estimate and its associated covariance forward in time. This prediction is based on the system's dynamics and is subject to process noise, which accounts for uncertainties in the model and the process itself. Following the prediction, the update step incorporates new measurements to correct the predicted state and covariance. This correction is achieved by calculating the Kalman gain, which determines the weight given to the new measurement based on the estimated uncertainties in both the prediction and the measurement (represented by the measurement noise). The difference between the actual measurement and the measurement predicted based on the current state estimate (the innovation) is then used to refine the state and reduce the uncertainty in the estimate. A key aspect of the EKF is its ability to handle non-linear systems by linearizing the non-linear process and measurement models around the current state estimate using Jacobian matrices. This linearization allows the application of Kalman filter principles to non-linear problems. We suppose $\hat{(\cdot)}$ as the visual-inertial fusion related values, $\tilde{(\cdot)}$ as the only inertial related values.

A. Extended Kalman Filter

To effectively estimate 3D rotation using an EKF, a suitable representation of the object's orientation must be chosen. Sev-

eral options are available, including euler angle, quaternion, and rotation matrix. Quaternions, specifically unit quaternions, offer a more compact and robust representation for 3D rotations, as well as avoiding gimbal lock and allowing for smooth interpolation.

Let the state vector at time t be:

$$\mathbf{x}_t = \begin{bmatrix} \mathbf{q}_t \\ \mathbf{b}_t \end{bmatrix} \quad (3)$$

where $\mathbf{q}_t = [q_w, q_x, q_y, q_z]^T$ is the unit quaternion representing the link's orientation.

Since the IMU gives orientation estimates, we assume the system follows a random walk for orientation

$$\begin{aligned} \mathbf{q}_{t+1} &= \mathbf{q}_t \otimes \delta \mathbf{q}_t \\ \mathbf{b}_{t+1} &= \mathbf{b}_t + \boldsymbol{\eta}_t^b \end{aligned} \quad (4)$$

where $\delta \mathbf{q}_t \approx [1, \frac{1}{2} \boldsymbol{\omega}_t \Delta t]$ is a small rotation quaternion representing random motion (as noise), $\boldsymbol{\eta}_t^b \sim \mathcal{N}(\mathbf{0}, Q_b)$ is the bias noise, \otimes is the quaternion product. For simplicity, since we don't use the IMU's angular velocity, the model can be represented as

$$\mathbf{q}_{t+1} = \mathbf{q}_t \otimes \mathbf{q}_{\text{noise}} \quad (5)$$

which can be linearized to

$$\mathbf{x}_{t+1} = f(\mathbf{x}_t) + \mathbf{w}_t = \begin{bmatrix} \mathbf{q}_t \otimes \delta \mathbf{q}_t \\ \mathbf{b}_t \end{bmatrix} + \mathbf{w}_t \quad (6)$$

with $\mathbf{w}_t = [q_{\text{noise}}, \boldsymbol{\eta}_t^b]$, where $f(\mathbf{x}_t) = \mathbf{x}_t$, \mathbf{w}_t is the drifting noise.

$$Q_t = \begin{bmatrix} Q_q & 0 \\ 0 & Q_b \end{bmatrix} \quad (7)$$

Measurement Models There are two types of observations, which is IMU measurement model

$$\mathbf{z}_t^{\text{imu}} = h^{\text{imu}}(\mathbf{x}_t) + \mathbf{v}_t^{\text{imu}} \quad (8)$$

with

$$h^{\text{imu}}(\mathbf{x}_t) = \mathbf{q}_t \otimes \delta \mathbf{q}(\mathbf{b}_t) \quad (9)$$

where $\delta \mathbf{q}(\mathbf{b}_t)$ represents a small rotation corresponding to the bias \mathbf{b}_t . For small angles, we approximate as

$$\delta \mathbf{q}(\mathbf{b}_t) \approx \left[1, \frac{1}{2} \mathbf{b}_t \right] \quad (10)$$

The camera measurement model

$$\mathbf{z}_t^{\text{cam}} = h^{\text{cam}}(\mathbf{x}_t) + \mathbf{v}_t^{\text{cam}} = \mathbf{q}_t + \mathbf{v}_t^{\text{cam}} \quad (11)$$

where $\mathbf{z}_t^{\text{imu}}$ and $\mathbf{z}_t^{\text{cam}}$ are estimated quaternions by the IMU and camera, $\mathbf{v}_t^{\text{imu}} \sim \mathcal{N}(0, R_{\text{imu}})$ and $\mathbf{v}_t^{\text{cam}} \sim \mathcal{N}(0, R_{\text{cam}})$ are small measurement noises.

Prediction Stage The prediction is running with the same frequency as the IMU data reading. Let the $\hat{\mathbf{x}}_{t|t}$ be the current state estimated in the current time step, $\hat{\mathbf{x}}_{t+k|t}$ be the state after k steps estimated in the current time step, $P_{t|t}$ be the current state covariance estimated in the current time, $P_{t+k|t}$ be the covariance after k steps estimated in the current time,

$$\begin{aligned} \hat{\mathbf{q}}_{t+1|t} &= \hat{\mathbf{q}}_{t|t} \otimes \delta \mathbf{q}_t \\ \hat{\mathbf{b}}_{t+1|t} &= \hat{\mathbf{b}}_{t|t} \end{aligned} \quad (12)$$

Assuming small rotation increments, we have

$$\hat{\mathbf{x}}_{t+1|t} = f(\hat{\mathbf{x}}_{t|t}) = \begin{bmatrix} \hat{\mathbf{q}}_{t+1|t} \\ \hat{\mathbf{b}}_{t+1|t} \end{bmatrix} = \hat{\mathbf{x}}_{t|t} \quad (13)$$

The state covariance is updated by

$$P_{t+1|t} = F_t P_{t|t} F_t^\top + Q_t \quad (14)$$

where F_t is the Jacobian of $f(\mathbf{x})$ with respect to \mathbf{x} , $F_t \approx I$, Q_t is the process noise covariance.

Update Stage Update stage is followed with the prediction stage. In general, when the measurement received, update the related states and parameters by

$$\begin{aligned} K_t &= P_{t|t-1} H_t^\top (H_t P_{t|t-1} H_t^\top + R)^{-1} \\ \hat{\mathbf{x}}_{t|t} &= \hat{\mathbf{x}}_{t|t-1} + K_t (\mathbf{z}_t - h(\hat{\mathbf{x}}_{t|t-1})) \\ P_{t|t} &= (I - K_t H_t) P_{t|t-1} \end{aligned} \quad (15)$$

The measurement function for the IMU is

$$h^{\text{imu}}(\mathbf{x}_t) = \mathbf{q}_t \otimes \left[1, \frac{1}{2} \mathbf{b}_t \right] \quad (16)$$

To perform the EKF update for IMU, linearizing the measurement function h^{imu} get

$$H_t^{\text{imu}} = \left. \frac{\partial h^{\text{imu}}}{\partial \mathbf{x}} \right|_{\hat{\mathbf{x}}_{t|t-1}} \quad (17)$$

which is then substitute with the R in Eq. 15 to update states.

To perform the EKF update for camera, as $h^{\text{cam}}(\mathbf{x}_t) = \mathbf{q}_t$, its Jacobian will be

$$H_t^{\text{cam}} \approx \begin{bmatrix} I_{4 \times 4} & 0_{4 \times 3} \end{bmatrix} \quad (18)$$

To perform the EKF update for both camera and IMU, the measurement model can be written as

$$\mathbf{z}_t = \begin{bmatrix} \mathbf{z}_t^{\text{cam}} \\ \mathbf{z}_t^{\text{imu}} \end{bmatrix} = \begin{bmatrix} H_t^{\text{cam}} \\ H_t^{\text{imu}} \end{bmatrix} \mathbf{x}_t + \begin{bmatrix} \mathbf{v}_t^{\text{cam}} \\ \mathbf{v}_t^{\text{imu}} \end{bmatrix} \quad (19)$$

while $R = \text{diag}(R^{\text{cam}}, R^{\text{imu}})$.

Finally, to maintain the unit norm of the quaternions,

$$\hat{\mathbf{x}}_{t|t} \leftarrow \frac{\hat{\mathbf{x}}_{t|t}}{\|\hat{\mathbf{x}}_{t|t}\|} \quad (20)$$

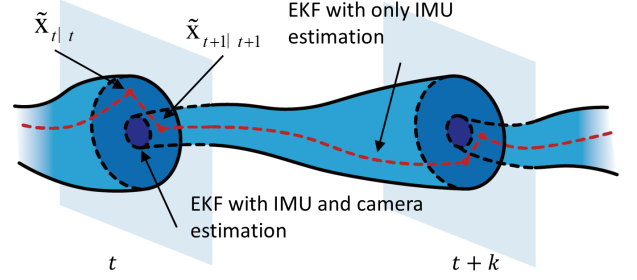


Fig. 5. Illustration of visual-inertial updates within the EKF. Due to drift bias in IMU measurements, the inertial estimate diverges over time. Although visual estimation has latency, retrospective corrections can be applied to states from k steps before the current time, allowing recomputation of the observation trajectory with higher accuracy.

B. Adaptation to Latency

The proprioception, as a low-level perception feedback signal, requires a real-time update frequency. However, the visual-based algorithm always lack of real-time capability, especially when running under learning-based algorithms. Therefore, to solve this problem, while maintain the advantage of EKF's improved estimation robustness and accuracy, we revised the EKF to a latency free method.

We use real-time IMU data to continuously predict and update the pose trajectory. When a delayed visual frame arrives at timestep t and this frame's inertial-visual EKF estimation arrives at timestep $t+k$, the EKF retrospectively refines the entire estimation from t to $t+k$, where k is the latency. This approach yields a more accurate estimation at $t+k$ than relying solely on inertial data (Fig. 5) as below.

$$\begin{aligned} \hat{\mathbf{x}}_{t+1|t+k}^- &= \tilde{\mathbf{x}}_{t|t+k} \\ \hat{P}_{t+1|t+k}^- &= F_t \tilde{P}_{t|t+k} F_t^\top + Q_t \\ \hat{K}_{t+1|t+k} &= \hat{P}_{t+1|t+k} \tilde{H}_{t+1}^\top (\tilde{H}_{t+1} \hat{P}_{t+1|t+k} \tilde{H}_{t+1}^\top + R)^{-1} \\ \hat{\mathbf{x}}_{t+1|t+k} &= \hat{\mathbf{x}}_{t+1|t+k}^- + \hat{K}_{t+1} (\tilde{\mathbf{z}}_{t+1}^{\text{imu}} - \tilde{H}_{t+1}^{\text{imu}} \hat{\mathbf{x}}_{t+1|t+k}^-) \\ \tilde{P}_{t+1|t+k} &= (I - \hat{K}_{t+1|t+k} \tilde{H}_{t+1}^{\text{imu}}) \hat{P}_{t+1|t+k}^- \end{aligned}$$

where $\hat{\mathbf{x}}_{t|t+k}$, $\hat{P}_{t|t+k}$, and $\hat{K}_{t|t+k}$ are the visual-inertial state, covariance, and Kalman gain at timestep t estimated at $t+k$. Based on this, we can refit all the prediction and updates using inertial information by

$$\begin{aligned} \tilde{\mathbf{x}}_{t+1|t} &= \hat{\mathbf{x}}_{t|t} \\ \tilde{P}_{t+1|t} &= F_t \hat{P}_{t|t} F_t^\top + Q_t \\ \tilde{K}_{t+1} &= \tilde{P}_{t+1|t} \tilde{H}_t^\top (\tilde{H}_t \tilde{P}_{t+1|t} \tilde{H}_t^\top + R)^{-1} \\ \tilde{\mathbf{x}}_{t+1|t+1} &= \tilde{\mathbf{x}}_{t+1|t} + \tilde{K}_{t+1} (\tilde{\mathbf{z}}_{t+1}^{\text{imu}} - \tilde{H}_{t+1}^{\text{imu}} \tilde{\mathbf{x}}_{t+1|t}) \\ \tilde{P}_{t+1|t+1} &= (I - \tilde{K}_{t+1} \tilde{H}_{t+1}^{\text{imu}}) \tilde{P}_{t+1|t} \end{aligned} \quad (21)$$

C. Solve the Configuration Space

Given the pose as rotation matrix, we need to solve the joint angles of the dexterous hand [30], which can be formulated

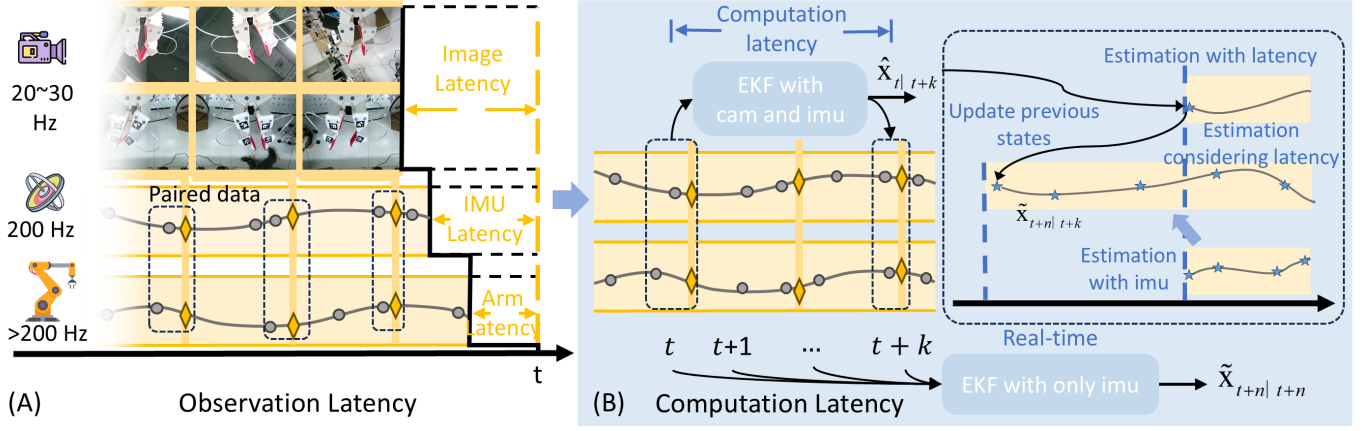


Fig. 6. The latency free EKF. There are two resources of latency, which are observation latency and computation latency. (A) shows observation latency between different input for attaining proprioception. (B) Computation latency is the major latency during EKF estimation. Therefore, we use IMU to conduct update and get real-time output, while use visual-inertial fusion to update states from $\hat{\mathbf{x}}_{t|t+k}$ to the current state $\hat{\mathbf{x}}_{t+k|t+k}$.

Algorithm 1 Solve the Unique Configuration Space from Rotation Matrix

Require: $\mathbf{R}_t, \alpha_{t-1}, \beta_{t-1}, \gamma_{t-1}$ ▷ rotation matrix, euler angles

Ensure: Euler angles $\alpha_t, \beta_t, \gamma_t$ is uniquely attained given

```

 $\mathbf{R}_t = Z_\alpha Y_\beta X_\gamma$ 
1: if  $R_{31} \neq \pm 1$  then
2:    $\beta_{t,1} = -\arcsin R_{31}$ 
3:    $\beta_{t,2} = \pi + \arcsin R_{31}$ 
4:   if  $|\beta_{t-1} - \beta_{t,1}| \leq |\beta_{t-1} - \beta_{t,2}|$  then
5:      $\beta_t \leftarrow \beta_{t,1}$ 
6:   else
7:      $\beta_t \leftarrow \beta_{t,2}$ 
8:   end if
9:    $\alpha_t \leftarrow \text{atan2}(\frac{R_{21}}{\cos \beta_t}, \frac{R_{11}}{\cos \beta_t})$ 
10:   $\gamma_t \leftarrow \text{atan2}(\frac{R_{32}}{\cos \beta_t}, \frac{R_{33}}{\cos \beta_t})$ 
11: else
12:   $\alpha_t \leftarrow \alpha_{t-1}$ 
13:  if  $\beta_t = \frac{\pi}{2}$  then
14:     $\gamma_t \leftarrow \alpha_t + \text{atan2}(R_{12}, R_{13})$ 
15:  else
16:     $\gamma_t \leftarrow -\alpha_t + \text{atan2}(-R_{12}, -R_{13})$ 
17:  end if
18: end if

```

as solving

$$\bar{\mathbf{R}}(\mathbf{z}_t) = \mathbf{R}_i(\theta) \mathbf{R}_j \mathbf{R}_k(\phi) \quad (22)$$

where $i, j, k \in \{x, y, z\}$, \mathbf{R}_j is a constant rotation matrix, θ and ϕ are the joint angles to be solved. To avoid dual solutions, we have the algorithm 1. A detailed table about different rotation sequence can also refer to the Appendix A.

VI. EXPERIMENTAL VERIFICATION

In this section, we validate the feasibility and reliability of using IMUs to measure joint angles. We compare the performance of three pose estimation approaches: *inertial-only*, *visual-only*, and *visual-inertial fusion*. Results demon-

strate that our method exhibits accurate dynamic estimation and robust performance in motion-rich scenarios.

TABLE I
FIRST-ORDER DRIFT (IN $\times 10^{-4}^\circ/\text{s}$) AND ANGULAR VARIANCE

Pose	#1	#2	#3	#4	#5	#6
Roll	-1	33	0	-24	0	0
Pitch	0	0	0	0	0	1
Yaw	-8	-36	-1	0	-6	1
Var (deg ²)	0.21	8.21	0.38	6.98	0.32	2.44

A. IMU System Validation

The static stability of the IMU measuring and the uniformity of 9-axis IMUs are validated in this section. The uniformity measures in which extent can we use a common base frame for different 9-axis IMUs. A common base frame will greatly reduce the difficulty in calibration for multiple IMUs systems.

1) *Stability of Inertial measurement*: In the static stability experiment, four IMUs were placed in six different orientations (Fig.7A). After calibration under high-confidence condition, data were collected continuously over a two-hour period. The mean first-order drift (in degrees per second) across different chips is summarized in Table I. Results show minimal drift following application of a normal kalman filter, and no significant directional bias is observed.

2) *Uniformity of 9-axis IMU*: Similar to the stability experiment, the uniformity experiment placed 4 IMUs in those six directions 7A. Considering quaternion is continuous in its range, thus reasonable to get interpolation, we use quaternion to get the mean variance and avoid the gimbal lock. Let each unit quaternion measurement be represented as $\mathbf{q}_i \in \mathbb{H}$, for $i = 1, 2, \dots, N$, where N is the number of measurements for a given pose. The mean quaternion \mathbf{q}_{mean} is attained by minimizing the sum of squared geodesic distances on the rotation group $\text{SO}(3)$,

$$\mathbf{q}_{\text{mean}} = \arg \min_{\mathbf{q}} \sum_{i=1}^N d_{\text{SO}(3)}^2(\mathbf{q}, \mathbf{q}_i)$$

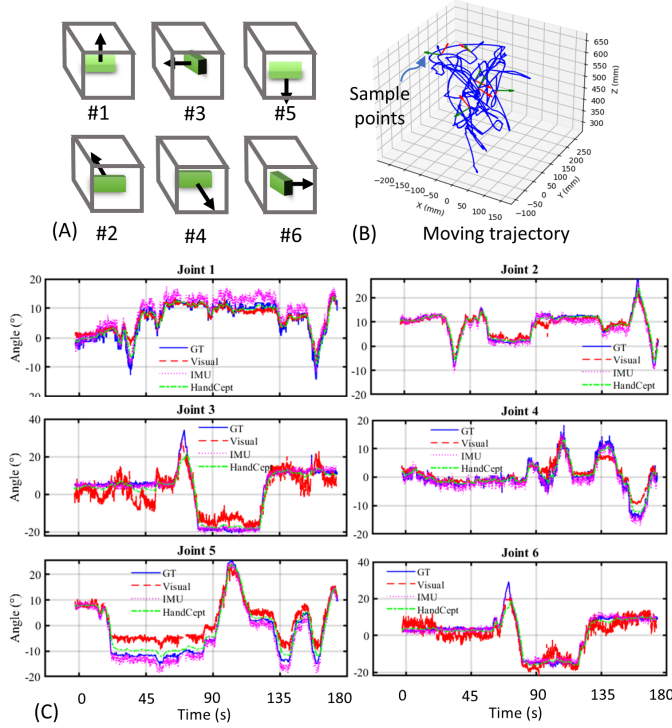


Fig. 7. Experimental results. (A) Placement and z-axis orientations used during IMU system verification. (B) Trajectory of the robot arm’s end-effector under teleoperated random motion. The coordinate frames represent sampled end-effector poses on the point of the trajectory. Both position and rotation are random during teleoperation. (C) Comparison of joint angle estimation across different methods. Joints 1, 2, and 3 correspond to the lateral, proximal, and distal joints of the left finger, respectively, while joints 4, 5, and 6 correspond to those of the right finger.

Then, the angular variance are obtained

$$\begin{aligned} \delta \mathbf{q}_i &= \mathbf{q}_i \cdot \mathbf{q}_{\text{mean}}^{-1} \\ \theta_i &= 2 \cdot \arccos(|w_i|) \\ \text{Var}(\theta) &= \frac{1}{N} \sum_{i=1}^N (\theta_i - \bar{\theta})^2 \end{aligned} \quad (23)$$

where w_i is the scalar part of $\delta \mathbf{q}_i$, $\text{Var}(\theta)$ is the variance. The mean variance in different direction are shown in Table. I. It’s obvious that the variance is very small therefore is reasonable to use a common base for different 9-axis IMUs. The greatest variance happens when the z-axis is perpendicular to the gravity direction.

B. Configuration Estimation Results

We use our previously developed DexCo hand [8], which lacks an onboard joint estimation system, to test HandCept. While earlier methods relied purely on inertial data and required complex calibration, they suffered from long-term drift during dynamic motion. Here, we validate the HandCept framework using three modes: IMU-only, visual-only, and visual-inertial joint angle estimation.

The experimental setup is illustrated in Fig.1A. The robot arm and dexterous hand are teleoperated to freely explore the workspace. Fig.1B and Fig. 1C depict a typical deployment using one camera and the IMU system. For evaluation, an

additional overhead camera is used to capture ground truth poses using ArUco markers.

During trials, the robot moves randomly throughout its workspace, ensuring diverse motion and viewpoint coverage. Fig.7B shows the end-effector’s 3D trajectory, which spans approximately half of a spherical volume, with directional variation at fixed positions to test sensitivity. A comparative plot in Fig.7C shows the ground truth trajectory alongside estimates from each method. HandCept demonstrates superior performance, effectively resisting drift and achieving higher accuracy than either single-modality approach.

VII. CONCLUSION AND FUTURE WORK

This work introduces HandCept, a novel visual-inertial proprioception framework for dexterous hands—addressing limitations not previously resolved in the literature. HandCept estimates joint angles using a zero-shot visual-inertial approach, combining IMU readings and synthetic visual pose predictions within a latency-compensated EKF. We validate HandCept through two primary experiments. First, we demonstrate that 9-axis IMUs exhibit stable and uniform behavior across multiple orientations, enabling shared-base calibration and reducing setup complexity. Second, we show that HandCept achieves state-of-the-art accuracy, with joint angle errors maintained between 2° to 4° without observable drift.

In the future, we have three directions. Firstly, an improved real-time property both for the visual estimation algorithm and EKF estimation algorithm will be made. Secondly, visual estimation with a fine-tune technique should be introduced for a better stability. Thirdly, other perception components should be included such as torque, compliance, and tactile.

APPENDIX A

ATTAINED EULER ANGLE FROM ROTATION MATRIX

REFERENCES

- [1] F. Zeng, W. Gan, Y. Wang, N. Liu, and P. S. Yu, “Large language models for robotics: A survey,” *arXiv preprint arXiv:2311.07226*, 2023.
- [2] C. Laschi, B. Mazzolai, and M. Cianchetti, “Soft robotics: Technologies and systems pushing the boundaries of robot abilities,” *Science robotics*, vol. 1, no. 1, p. eaah3690, 2016.
- [3] M. T. Mason, “Toward robotic manipulation,” *Annual Review of Control, Robotics, and Autonomous Systems*, vol. 1, no. 1, pp. 1–28, 2018.
- [4] A. Billard and D. Kragic, “Trends and challenges in robot manipulation,” *Science*, vol. 364, no. 6446, p. eaat8414, 2019.
- [5] J. Cui and J. Trinkle, “Toward next-generation learned robot manipulation,” *Science robotics*, vol. 6, no. 54, p. eabd9461, 2021.
- [6] A. M. Dollar, A. Bicchi, M. R. Cutkosky, and R. D. Howe, “Special issue on the mechanics and design of robotic hands,” pp. 675–676, 2014.
- [7] C. Chi, Z. Xu, C. Pan, E. Cousineau, B. Burchfiel, S. Feng, R. Tedrake, and S. Song, “Universal manipulation interface: In-the-wild robot teaching without in-the-wild robots,” *arXiv preprint arXiv:2402.10329*, 2024.
- [8] J. Zhou, J. Huang, Q. Dou, P. Abeel, and Y. Liu, “A dexterous and compliant (dexco) hand based on soft hydraulic actuation for human inspired fine in-hand manipulation,” *IEEE Transactions on Robotics*, 2024.
- [9] J. Zhou, Y. Chen, Y. Hu, Z. Wang, Y. Li, G. Gu, and Y. Liu, “Adaptive variable stiffness particle phalange for robust and durable robotic grasping,” *Soft Robotics*, vol. 7, no. 6, pp. 743–757, 2020.
- [10] J. Zhou, X. Chen, U. Chang, J. T. Lu, C. C. Y. Leung, Y. Chen, and Z. Wang, “A soft-robotic approach to anthropomorphic robotic hand dexterity,” *IEEE Access*, vol. 7, pp. 101 483–101 495, 2019.
- [11] S. Yuan, A. D. Epps, J. B. Nowak, and J. K. Salisbury, “Design of a roller-based dexterous hand for object grasping and within-hand manipulation,” in *2020 IEEE International Conference on Robotics and Automation (ICRA)*. IEEE, 2020, pp. 8870–8876.

TABLE II
SUMMARY OF EULER ANGLE SOLUTIONS

Proper Euler angles		Tait–Bryan angles	
Gimbal Lock	$\beta = \frac{\pi}{2} \text{ or } \frac{3\pi}{2}$	Gimbal Lock	$\beta = \pm \frac{\pi}{2}$
$X_\alpha Z_\beta X_\gamma$	$\begin{cases} \beta_1 = \arccos R_{11} \\ \beta_2 = 2\pi - \arccos R_{11} \\ \alpha = \text{atan2}(\frac{R_{31}}{\sin \beta}, \frac{R_{21}}{\sin \beta}) \\ \gamma = \text{atan2}(\frac{R_{13}}{\sin \beta}, \frac{R_{12}}{-\sin \beta}) \end{cases}$	$X_\alpha Z_\beta Y_\gamma$	$\begin{cases} \beta_1 = -\arcsin R_{12} \\ \beta_2 = \pi + \arcsin R_{12} \\ \alpha = \text{atan2}(\frac{R_{32}}{\cos \beta}, \frac{R_{22}}{\cos \beta}) \\ \gamma = \text{atan2}(\frac{R_{13}}{\cos \beta}, \frac{R_{11}}{\cos \beta}) \end{cases}$
$X_\alpha Y_\beta X_\gamma$	$\begin{cases} \beta_1 = \arccos R_{11} \\ \beta_2 = 2\pi - \arccos R_{11} \\ \alpha = \text{atan2}(\frac{R_{31}}{\sin \beta}, \frac{R_{21}}{\sin \beta}) \\ \gamma = \text{atan2}(\frac{R_{13}}{\sin \beta}, \frac{R_{12}}{-\sin \beta}) \end{cases}$	$X_\alpha Y_\beta Z_\gamma$	$\begin{cases} \beta_1 = -\arcsin R_{12} \\ \beta_2 = \pi + \arcsin R_{12} \\ \alpha = \text{atan2}(\frac{R_{32}}{\cos \beta}, \frac{R_{22}}{\cos \beta}) \\ \gamma = \text{atan2}(\frac{R_{13}}{\cos \beta}, \frac{R_{11}}{\cos \beta}) \end{cases}$
$Y_\alpha X_\beta Y_\gamma$	$\begin{cases} \beta_1 = \arccos R_{11} \\ \beta_2 = 2\pi - \arccos R_{11} \\ \alpha = \text{atan2}(\frac{R_{31}}{\sin \beta}, \frac{R_{21}}{\sin \beta}) \\ \gamma = \text{atan2}(\frac{R_{13}}{\sin \beta}, \frac{R_{12}}{-\sin \beta}) \end{cases}$	$Y_\alpha X_\beta Z_\gamma$	$\begin{cases} \beta_1 = -\arcsin R_{12} \\ \beta_2 = \pi + \arcsin R_{12} \\ \alpha = \text{atan2}(\frac{R_{32}}{\cos \beta}, \frac{R_{22}}{\cos \beta}) \\ \gamma = \text{atan2}(\frac{R_{13}}{\cos \beta}, \frac{R_{11}}{\cos \beta}) \end{cases}$
$Y_\alpha Z_\beta Y_\gamma$	$\begin{cases} \beta_1 = \arccos R_{11} \\ \beta_2 = 2\pi - \arccos R_{11} \\ \alpha = \text{atan2}(\frac{R_{31}}{\sin \beta}, \frac{R_{21}}{\sin \beta}) \\ \gamma = \text{atan2}(\frac{R_{13}}{\sin \beta}, \frac{R_{12}}{-\sin \beta}) \end{cases}$	$Y_\alpha Z_\beta X_\gamma$	$\begin{cases} \beta_1 = -\arcsin R_{12} \\ \beta_2 = \pi + \arcsin R_{12} \\ \alpha = \text{atan2}(\frac{R_{32}}{\cos \beta}, \frac{R_{22}}{\cos \beta}) \\ \gamma = \text{atan2}(\frac{R_{13}}{\cos \beta}, \frac{R_{11}}{\cos \beta}) \end{cases}$
$Z_\alpha Y_\beta Z_\gamma$	$\begin{cases} \beta_1 = \arccos R_{11} \\ \beta_2 = 2\pi - \arccos R_{11} \\ \alpha = \text{atan2}(\frac{R_{31}}{\sin \beta}, \frac{R_{21}}{\sin \beta}) \\ \gamma = \text{atan2}(\frac{R_{13}}{\sin \beta}, \frac{R_{12}}{-\sin \beta}) \end{cases}$	$Z_\alpha Y_\beta X_\gamma$	$\begin{cases} \beta_1 = -\arcsin R_{12} \\ \beta_2 = \pi + \arcsin R_{12} \\ \alpha = \text{atan2}(\frac{R_{32}}{\cos \beta}, \frac{R_{22}}{\cos \beta}) \\ \gamma = \text{atan2}(\frac{R_{13}}{\cos \beta}, \frac{R_{11}}{\cos \beta}) \end{cases}$
$Z_\alpha X_\beta Z_\gamma$	$\begin{cases} \beta_1 = \arccos R_{11} \\ \beta_2 = 2\pi - \arccos R_{11} \\ \alpha = \text{atan2}(\frac{R_{31}}{\sin \beta}, \frac{R_{21}}{\sin \beta}) \\ \gamma = \text{atan2}(\frac{R_{13}}{\sin \beta}, \frac{R_{12}}{-\sin \beta}) \end{cases}$	$Z_\alpha X_\beta Y_\gamma$	$\begin{cases} \beta_1 = -\arcsin R_{12} \\ \beta_2 = \pi + \arcsin R_{12} \\ \alpha = \text{atan2}(\frac{R_{32}}{\cos \beta}, \frac{R_{22}}{\cos \beta}) \\ \gamma = \text{atan2}(\frac{R_{13}}{\cos \beta}, \frac{R_{11}}{\cos \beta}) \end{cases}$

- [12] L. U. Odhner, L. P. Jentoft, M. R. Claffee, N. Corson, Y. Tenzer, R. R. Ma, M. Buehler, R. Kohout, R. D. Howe, and A. M. Dollar, “A compliant, underactuated hand for robust manipulation,” *The International Journal of Robotics Research*, vol. 33, no. 5, pp. 736–752, 2014.
- [13] K. Shaw, A. Agarwal, and D. Pathak, “Leap hand: Low-cost, efficient, and anthropomorphic hand for robot learning,” *arXiv preprint arXiv:2309.06440*, 2023.
- [14] T. Chen, M. Tippur, S. Wu, V. Kumar, E. Adelson, and P. Agrawal, “Visual dexterity: In-hand dexterous manipulation from depth,” in *IcmI workshop on new frontiers in learning, control, and dynamical systems*, 2023.
- [15] M. Quigley, C. Salisbury, A. Y. Ng, and J. K. Salisbury, “Mechatronic design of an integrated robotic hand,” *The International Journal of Robotics Research*, vol. 33, no. 5, pp. 706–720, 2014.
- [16] M. Ciocarlie, F. M. Hicks, R. Holmberg, J. Hawke, M. Schlicht, J. Gee, S. Stanford, and R. Bahadur, “The velo gripper: A versatile single-actuator design for enveloping, parallel and fingertip grasps,” *The International Journal of Robotics Research*, vol. 33, no. 5, pp. 753–767, 2014.
- [17] M. A. Riza, Y. I. Go, S. W. Harun, and R. R. Maier, “Fbg sensors for environmental and biochemical applications—a review,” *IEEE sensors journal*, vol. 20, no. 14, pp. 7614–7627, 2020.
- [18] J. Kang, S. Lee, and Y.-L. Park, “Soft bending actuator with fiber-jamming variable stiffness and fiber-optic proprioception,” *IEEE Robotics and Automation Letters*, vol. 8, no. 11, pp. 7344–7351, 2023.
- [19] J. Huang, J. Zhou, Z. Wang, J. Law, H. Cao, Y. Li, H. Wang, and Y. Liu, “Modular origami soft robot with the perception of interaction force and body configuration,” *Advanced Intelligent Systems*, vol. 4, no. 9, p. 2200081, 2022.
- [20] A. B. Dawood, H. Godaba, A. Ataka, and K. Althoefer, “Silicone-based capacitive e-skin for exteroception and proprioception,” in *2020 IEEE/RSJ International Conference on Intelligent Robots and Systems (IROS)*. IEEE, 2020, pp. 8951–8956.
- [21] M. D. Mitchell, F. E. Hurley, and C. D. Onal, “Fast probabilistic 3-d curvature proprioception with a magnetic soft sensor,” in *2021 IEEE 17th International Conference on Automation Science and Engineering (CASE)*. IEEE, 2021, pp. 215–220.
- [22] L. Cong, H. Liang, P. Ruppel, Y. Shi, M. Görner, N. Hendrich, and J. Zhang, “Reinforcement learning with vision-proprioception model for robot planar pushing,” *Frontiers in Neurorobotics*, vol. 16, p. 829437, 2022.
- [23] T. Helps and J. Rossiter, “Proprioceptive flexible fluidic actuators using conductive working fluids,” *Soft robotics*, vol. 5, no. 2, pp. 175–189, 2018.
- [24] D. Alatorre, D. Axinte, and A. Rabani, “Continuum robot proprioception: the ionic liquid approach,” *IEEE Transactions on Robotics*, vol. 38, no. 1, pp. 526–535, 2021.
- [25] L. Teixeira, F. Maffra, M. Moos, and M. Chli, “Vi-rpe: Visual-inertial relative pose estimation for aerial vehicles,” *IEEE Robotics and Automation Letters*, vol. 3, no. 4, pp. 2770–2777, 2018.
- [26] S. Chen, Y. Feng, C.-Y. Wen, Y. Zou, and W. Chen, “Stereo visual inertial pose estimation based on feedforward and feedbacks,” *IEEE/ASME Transactions on Mechatronics*, vol. 28, no. 6, pp. 3562–3572, 2023.
- [27] N. Guedri and R. Gharbi, “Finger movements tracking of the human hand using the smart camera to control the allegro hand robot,” in *2021 IEEE 2nd International Conference on Signal, Control and Communication (SCC)*. IEEE, 2021, pp. 320–324.
- [28] T. Li and H. Yu, “Visual-inertial fusion-based human pose estimation: A review,” *IEEE Transactions on Instrumentation and Measurement*, vol. 72, pp. 1–16, 2023.
- [29] Y. He, H. Huang, H. Fan, Q. Chen, and J. Sun, “Ffb6d: A full flow bidirectional fusion network for 6d pose estimation,” in *Proceedings of the IEEE/CVF conference on computer vision and pattern recognition*, 2021, pp. 3003–3013.
- [30] G. G. Slabaugh, “Computing euler angles from a rotation matrix,” *Retrieved on August*, vol. 6, no. 2000, pp. 39–63, 1999.